JOURNAL OF PLANKTON RESEARCH | VOLUME 28 | NUMBER 5 | PAGES 509–522 | 2006

Laboratory studies of predator–prey encounters in turbulent environments: effects of changes in orientation and field of view

J. MANN[1], S. OTT[1], H. L. PÉCSELI[2,3]* AND J. TRULSEN[2,4]

[1]RISØ NATIONAL LABORATORY, DK-4000 ROSKILDE, DENMARK, [2]CENTRE FOR ADVANCED STUDY, DRAMMENSVEIEN 78, N-0271 OSLO, NORWAY, [3]INSTITUTE OF PHYSICS, UNIVERSITY OF OSLO, BOX 1048 BLINDERN, N-0316 OSLO, NORWAY AND [4]INSTITUTE OF THEORETICAL ASTROPHYSICS, UNIVERSITY OF OSLO, BOX 1029 BLINDERN, N-0315 OSLO, NORWAY

*CORRESPONDING AUTHOR: hans.pecseli@fys.uio.no

Received October 18, 2005; accepted in principle December 14, 2005; accepted for publication February 6, 2006; published online February 9, 2006

Communicating editor: K.J. Flynn

Small polystyrene particles were used to represent aquatic micro-organisms on millimeter scales, assuming small or negligible self-induced motions. A large number of such particles were released in turbulent flows that were generated in a controlled laboratory experiment, where the turbulence parameters were reproducible and could be kept constant over extended times. These polystyrene particles are tracked by video techniques. The available database allows estimates of the equivalents of planktonic contact rates in the turbulent flow. The results are expressed in terms of average prey fluxes. Scaling laws for the average contact rates for different turbulence intensities and for varying ranges of interception of the predators and also for different forms of the fields of view were analyzed, using two models for the orientation with respect to the flow. Irrespective of orientation and shape of the volume of interception, the scaling with the turbulence intensity is weak, while the variations with the range of perception are significant. The scaling laws obtained by this procedure have universal validity, and they are applicable also for conditions in nature. The sole restriction is that the range of predator perception is within the universal subrange.

INTRODUCTION

The rate of encounter between predators and prey is considered to be a key determinant of vital rates of many planktonic organisms. In particular, turbulent mixing is found to be important for the feeding process of such aquatic micro-organisms by controlling the contact rate between predators and prey (Rothschild and Osborn, 1988; Mauchline, 1998). The observation has found analytic (Gerritsen and Strickler, 1977; Muelbert *et al.* 1994; Osborn, 1996) as well as experimental support by observations of micro-organisms in turbulent environments (Sundby and Fossum, 1990; Kiørboe and MacKenzie, 1995). The effect depends on the turbulence level and the food concentration, which is related to the local environment, and to the perceptive field of the predator. The latter may vary in geometry both in size and shape between species, and for one species there may also be ontogeny effects (i.e. age/size-dependent effects). Many previous studies model predator–prey encounters by assuming that the former possesses isotropic perception capabilities and consequently that their field of view can be modeled by a sphere, with a given radius R determined by the predators sensory system (see Fig. 1a). With this ideal symmetry, some results can be obtained analytically (Gerritsen and Strickler, 1977; Osborn, 1996), and also by simple dimensional arguments (Mann *et al.*, 2005). For this case, it can thus be demonstrated that the average asymptotic prey flux to a predator embedded in homogeneous isotropic three-dimensional turbulence scales as $n_0\varepsilon^{1/3}R^{7/3}$, apart from a numerical constant, which was experimentally found to be in the range 5–10 (Mann *et al.*, 2005). The average energy dissipated per unit mass fluid is here given as ε, while n_0 is the reference prey concentration, see also list of symbols in Table I.

doi:10.1093/plankt/fbi136, available online at www.plankt.oxfordjournals.org

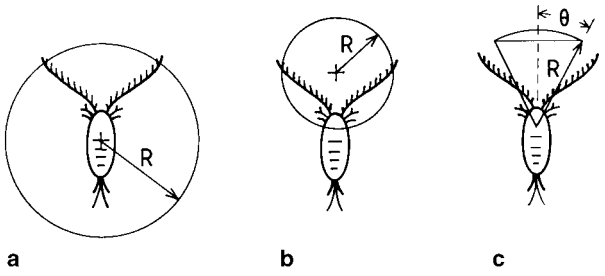

Fig. 1. Schematic presentation of fields of view for small aquatic micro-organisms.

Table I: List of the most important symbols

Quantity	Symbol	Unit
Energy dissipation per gram fluid	ε	mm^2s^{-3}
Taylor micro scale	λ	mm
Kolmogorov length scale	η	mm
Kolmogorov time scale	τ_η	s
Eddy turnover time	τ_F	s
Mean-square fluctuating velocity	$\langle u^2 \rangle$	$mm^2\ s^{-2}$
Root-mean-square of one velocity component	$\sigma = \sqrt{\langle u^2/3 \rangle}$	$mm\ s^{-1}$
Kinematic viscosity	ν	$mm^2\ s^{-1}$
Prey concentration	n	mm^{-3}

There are, however, a number of experimental studies which indicate that the assumption of a spherical field of view is in error, e.g. copepods perception capabilities can be strongly aligned with the orientation of their antennae, while visual predators such as fish larvae tend to see more forward and above, rather than behind. One could still argue for a spherical view as in Fig. 1b, which appears 'natural', but in this case the center of the sphere does not correspond to a position of a predator, which in our experiment is represented by a polystyrene particle.

In cases where the perceptive field is not spherical, the direction of orientation (e.g. angle of vision) relative to the local velocity field may affect the encounter rate. Small-scale turbulence has an isotropic chaotic nature, with no preferred velocity direction. It is not obvious what the consequences are for an organism with non-spherical perceptive fields. Does the orientation angle in such cases affect the encounter rate? Or do the chaotic turbulent motions average out the effect, so that the geometric shape of the field of view is irrelevant?

In this article we have investigated these problems in a laboratory experiment. Turbulent flows were generated in a tank by two moving grids, ensuring a homogeneous distribution of small-scale turbulence throughout the tank. The motion of small neutrally buoyant polystyrene particles, which represent passively moving plankton, was recorded by video. The chaotic orbit of individual 'plankton' particles could then be traced. We can consider one such particle as a predator. Other particles that come within a given 'perceptive field' associated with that predator can then take the role of prey. The encounter rate was then investigated for different radii, shapes and orientations of the perceptive field. The system allows for tracking of a large amount of particles simultaneously. Each of the particles can take the role of both predator and prey, allowing many realizations of the experiment, and thereby lower the uncertainty of the estimated average values.

We have previously studied the case with spherical capture volumes (Mann *et al.*, 2002, 2005). In the present study we attempt to relax some of the idealizations, by assuming conical fields of view, as illustrated in Fig. 1c, and consider different opening angles, θ, in the cone, and also different radii, R. Models have been suggested for the perception field of calanoid copepods where the field-of-view consists of two cones directed oppositely in the sidewise direction (Bundy *et al.*, 1998; Lewis, 2003). In such cases, our model can apply to one of these cones. Relaxing the simplifying assumption of spherical volumes, the problem has two new variables, the angle θ and the orientation of the cone with respect to the local flow velocity. Two limiting cases for the orientations of the cones were considered: one where the cone axis is prescribed with respect to a local frame of reference for the flow and one where it is prescribed in the laboratory frame. Evidently, by letting $\theta \rightarrow 180^\circ$, we recover the spherical case analyzed before (Mann *et al.*, 2002, 2005). The results summarized in the following can be seen as covering representative variations of the orientations of micro-organisms in turbulent velocity fields. The model for the field of view illustrated in Fig. 1c is of course also idealized (Browman, 1996; Bundy *et al.*, 1998), but has nonetheless been applied in several analytical studies (Lewis, 2003). The effects of non-spherical perception fields as related to fish larvae have been discussed explicitly by, for instance, Browman (Browman, 1996) and by a net energy gain (NEG) model also by Galbraith *et al.* (Galbraith *et al.*, 2004). The conical model adopted here remains an idealization, but it is more relevant for aquatic micro-organisms than the simple spherical model, and with the new free parameters introduced, it also requires a significantly more complicated data analysis.

When relating our results to average prey fluxes for aquatic micro-organisms in a turbulent environment, it is here implicitly assumed that prey is captured with certainty. More realistic conditions, with a finite capture probability (MacKenzie *et al.*, 1994), have been discussed

Table II: Summary of the parameters derived from the second-order structure function and the spectra obtained from it, based on measurements in the restricted volume shown in Fig. 2

L_E (mm)	σ (mm s^{-1})	L_{int} (mm)	ε (mm^2 s^{-3})	τ_η (s)	η (mm)	λ (mm)	R_λ
27	12	20	65	0.117	0.32	5.6	78
29	12	22	62	0.120	0.33	5.8	81
27	16	20	140	0.080	0.27	4.9	88
28	17	21	160	0.075	0.26	4.9	91
29	16	22	135	0.081	0.27	5.1	93
28	19	21	225	0.063	0.24	4.6	97
31	18	23	160	0.075	0.26	5.1	100
29	21	22	279	0.056	0.22	4.5	104

elsewhere for the special case of a spherical field of view (Mann *et al.*, 2003; Jørgensen *et al.*, 2005).

Our main results are obtained in the form of scaling laws, which are expected to have general validity for length scales within the universal subrange of the turbulence. The results can be seen as representative also in cases where the organisms possess a self-induced motion, as long as their velocities with respect to the surrounding flow are much smaller than a root-mean-square velocity, $\sqrt{\langle u^2\rangle} \equiv \sigma\sqrt{3}$, of the turbulent motions, see also the list of symbols given in Table I. To be precise, our analysis refers to an initial value problem, where a predator is released in a statistically homogeneous distribution of prey with given concentration n_0, which is our reference concentration. During the subsequent capture of prey, the average concentration is depleted in the vicinity of the predator, until finally a steady state situation develops, where the captured prey is, on average, substituted (or compensated) by the turbulent mixing in the flow.

Even though the flow conditions in the present experiment, as summarized in Table II, are rarely met in nature, the scaling laws obtained are assumed to have universal validity thus being applicable also for conditions in nature, within the parameter ranges of applicability. The restriction is that the turbulence is fully developed so that a universal subrange exists, and that the scale lengths R are within this subrange.

METHODS

The present study is based on experimental results obtained in a controlled laboratory experiment, where a turbulent flow with reproducible bulk parameters, such as the dissipated energy per gram fluid ε, could be obtained (Ott and Mann, 2000). As long as we may consider small predators and their prey to be passively moving with the flow, we can let them be represented by small neutrally buoyant polystyrene spheres, which are passively carried by the turbulent motions. Similarly, we let their prey be represented by similar polystyrene particles. The basic features of the present experiment are described elsewhere (Ott and Mann, 2000), with a detailed description given by Mann *et al.* (Mann *et al.*, 1999). A short summary will suffice here. The turbulence is generated by the motion of two plastic grids, in the top and bottom of a tank with $320 \times 320 \times 450$ mm^3 inner dimensions, see Fig. 2 for a schematic illustration. Typical Taylor micro-scale Reynolds numbers (Tennekes and Lumley, 1972; Hinze, 1975), $R_\lambda = \lambda^2/(\eta^2\sqrt{15})$, are $\sim$100 for the present conditions, using the Taylor micro-scale $\lambda = (15\nu\sigma^2/\varepsilon)^{1/2}$, where $\nu \approx 0.89$ mm^2 s^{-1} is the kinematic viscosity of the water, ε is the specific energy dissipation rate, and σ^2 is the variance of one velocity component. The Kolmogorov length scale $\eta \equiv (\nu^3/\varepsilon)^{1/4}$ is less than 1/2 mm for the present conditions, while Kolmogorov time scales $\tau_\eta \equiv (\nu/\varepsilon)^{1/2}$ are in the range 0.05–0.12 s. The 'micro-scale' η represents the length-scales, where the viscous effects become important, see also the summary given by Tennekes and Lumley (Tennekes and Lumley, 1972) concerning the physical meaning of the symbols. With the given size of the polystyrene particles, we are not able to resolve scales comparable to or smaller than η. A characteristic Eulerian length scale ('outer' scale), L_E as well as ε, are determined by fitting a von Kármán type wavenumber spectrum (Mann *et al.*, 1999; Ott and Mann, 2000) to experimentally obtained results. L_E is found to be in the range 20–25 mm. This outer scale determines the maximum separation between two points within the universal Kolmogorov subrange of the turbulence, while the Komogorov scale, η, sets the lower limit. Separations smaller than η fall within the dissipation subrange. An integral length scale can be defined by the integral of the parallel velocity component correlation function $R_{||}(r)$ as $L_{int} = \int R_{||}(r)dr$. A summary of

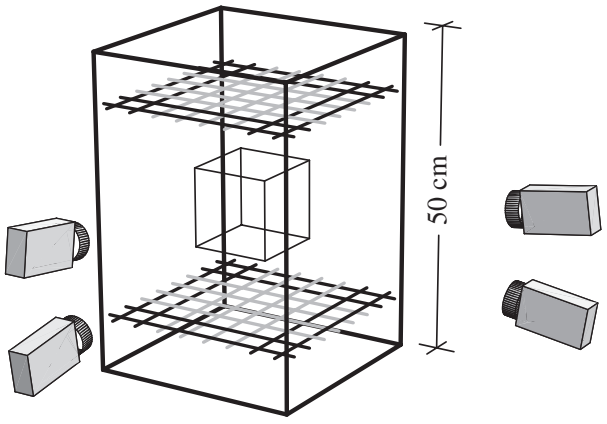

Fig. 2. Schematic illustration of the experimental set up, showing the movable grids and the four video cameras. A restricted measuring volume of 140 × 140 × 120 mm^3 is shown by thin lines.

parameters for eight different conditions used in the present work is given in Table II. The 'slippage' between spheres and the local flow is considered negligible (Mann *et al.*, 2005) for the present value of the Stokes number $<<0.05$.

The motions of small polystyrene particles of diameter a = 0.5–0.6 mm are followed with four video-cameras, and the simultaneous positions of typically 500–1000 particles recorded at time intervals of 1/25 s. For a very low density of test particles two cameras might suffice, but for the given density we found four cameras to give the best positioning (Mann *et al.*, 1999). The size of the effective measuring volume is approximately 140 × 140 × 120 mm^3. It is ensured that the particles used in the experiment are approximately neutrally buoyant, as described by Mann *et al.* (Mann *et al.*, 1999). By a tracking procedure it is possible to link the positions of particles (Mann *et al.*, 1999), and thus follow their individual motions in 3 spatial dimensions. In particular also their time varying local velocity can be deduced (Ott and Mann, 2000; Mann *et al.*, 2005). The longest observed track had duration of 40 s, but this is exceptional: usually the tracks can be followed for 1–2 s only. For two of the experiments (those with R_λ = 88 and 100, see Table II) we followed approximately 600 particles, for the rest approximately 1100 particles in the reference volume. These numbers correspond to particle densities of 2.5×10^{-4} particles mm^{-3} and 4.7×10^{-4} particles mm^{-3}, respectively. Such densities are too low to make the particles alter the general flow characteristics. We demonstrated before (Mann *et al.*, 2005) that the particles are uniformly distributed in a statistical sense, to a good approximation.

Experiments are carried out for different intensities of the turbulent velocity fluctuations, $\langle u^2 \rangle$. With the polystyrene particles acting as markers for the local flow velocities, experimental estimates can be obtained, for instance, for the second order structure function,

$$\Psi_2(r) \equiv \left\langle (u_r(0,t) - u_r(r,t))^2 \right\rangle \approx C_K(\varepsilon\, r)^{2/3}, \qquad (1)$$

with u_r here being the velocity component along the direction of r, with C_K being the Kolmogorov constant. We have $\Psi_2(r)$ being independent of t for time stationary conditions. We demonstrated (Ott and Mann, 2000; Mann *et al.*, 2005) the existence of a universal range up to separations close to L_E, defined before.

A large-scale mean flow can be observed in the experiment with a velocity up to 5.3 mm s^{-1} in the vertical direction and 2.8–4.5 mm s^{-1} in the two other directions. These values depend somewhat on the frequency of the grid oscillations (Mann *et al.*, 1999). Other methods for forcing the turbulence (Hwang and Eaton, 2004; Webster *et al.*, 2004) may give smaller mean flows, but the resulting turbulence levels are often smaller as well, and a universal subrange may not fully develop. For the ensuing Lagrangian analysis, this large-scale motion is immaterial, since both predator and prey are convected similarly by the large-scale motions. The present mean flow values should be compared to noticeably larger fluctuating velocities, see Table II. The uncertainty on the estimate of ε, in particular, is discussed by Mann *et al.* (Mann *et al.*, 1999); see also Mann *et al.* (Mann *et al.*, 2005).

The parameter values attained for the present experimental conditions are only marginally relevant for conditions in nature. Thus we have approximate values: for the open ocean $\{\varepsilon \sim 10^{-4} - 1\ mm^2\ s^{-2}; \eta \sim 10^{-1}\ mm\}$, the shelf $\{\varepsilon \sim 10^{-1} - 1\ mm^2\ s^{-2}; \eta \sim 2 - 1\ mm\}$, the coastal zone $\{\varepsilon \sim 10^{-1} - 10^{2}\ mm^2\ s^{-2}; \eta \sim 2 - 0.2\ mm\}$, and for the tidal front $\{\varepsilon \sim 10\ mm^2\ s^{-2}; \eta \sim 0.5\ mm\}$ (Granata and Dickey, 1991; Kiørboe and Saiz, 1995). Energy dissipation rates ε and Kolmogorov length scales η as those found in our experiment occur in nature only under strongly disturbed conditions. The turbulent time scales are also generally shorter in the experiment than in nature. The proposed scaling laws can, however, be tested under our conditions, and given the good agreement, these laws can then be safely applied to conditions which cannot be achieved in the experiment, provided the restrictions of relevant length scales being in the universal subrange is satisfied. For the previous list, the largest values of the Kolmogorov length can be larger than the relevant characteristic size of a region of interception. The range of radii R that we use is realistic: for herring larvae we have an estimated contact radius ~3 mm (for instance Blaxter and Staines, 1971; Lewis and Pedley, 2000). Within the applicability of a universal scaling-law, our results can be extrapolated to arbitrary contact radii.

RESULTS AND DISCUSSION

Particle fluxes into a moving volume

With the records for simultaneous particle trajectories being available, we can select one of them to represent the 'predator' and label all the others as 'prey'. We then select a radius R and opening angle θ in the volume of interception, and then remove all the particles which happen to be inside this volume at the initial time. During the subsequent Lagrangian motion of the reference 'predator', we count the number of prey entering its co-moving volume of interception between successive time steps. Each time a particle enters, it is 'eaten' in the sense that it is removed from the database. Physically, it is of course still there, but it is just not counted anymore. If the data analysis is carried out for very long times, all particles representing prey will eventually be removed. Here we are only interested in the time evolution of the prey flux for times up to an eddy turnover time. As long as R is much smaller than the size of the measuring volume, we can with negligible error assume the prey concentration to be constant at large distances, corresponding to an ideally infinite system. By choosing a large number of realizations, we can give an estimate for the ensemble averaged Lagrangian prey flux as a function of time after release.

We consider two cases for the angle between the local flow velocity and the direction specified by the cone-of-view. It turns out that some interesting (and maybe even counter-intuitive) results are found by letting this angle be zero. Another case is realized by letting the angle be randomly varying; this may be the case that is most relevant for phenomena in nature.

First we consider the case where the angle between the local flow vector and the symmetry line defined by the cone is constant, here taken to be zero. In the data analysis this is simple, since the local flow vector of the polystyrene particles is known at each sampling time. In Fig. 3 we show, with solid lines, examples of the time varying particle flux to a moving volume with a given radius R and opening angle $\theta = 90^\circ$. This flux is the result of a competition between, on one hand, the depletion of the density of polystyrene particles in the near vicinity of the reference volume as they are 'absorbed' and, on the other hand, inward flux of such particles, due to mixing by the turbulent motions in the flow. In each realization, we divide the flux by the initial particle density for that particular realization. The result thus represents the particle flux for unit particle density, i.e. 1 particle per mm^3. For radii much smaller than the length scale of the turbulence, $R << L_E$, we find that the flux level varies only weakly with time. A decreasing trend becomes more

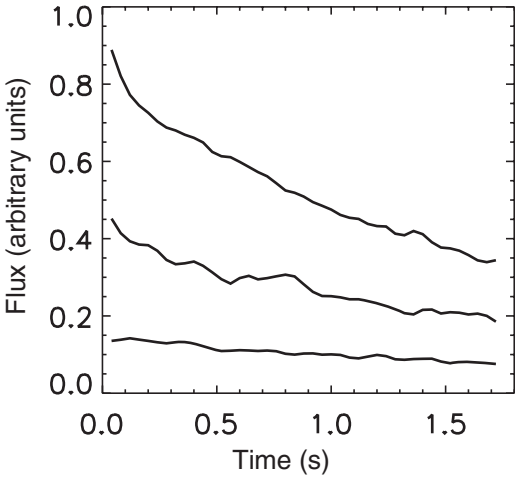

Fig. 3. Time variation of the flux to a moving conical volume, for different radii $R = 10$, 15 and 20 mm, a fixed opening angle $\theta = 90^\circ$, the cone axis being parallel to the local flow vector. Fluxes are in arbitrary units, but by multiplying the fluxes given by a factor 10^5, here and in the following, we obtain the flux that would be obtained if the density was 1 particle per mm^3. We have $\epsilon = 225$ mm^2 s^{-3}. For this condition we have the time $(R^2/\epsilon)^{1/3} = 1$ s for $R = 15$ mm. The irregularities of the individual curves represent the statistical uncertainty of the flux estimate.

conspicuous as the radius is increased, and for $R > L_E$ we find a significant flux reduction for increasing times. The flux is largest initially, when the concentration of 'prey' in the surrounding is largest. At later times there will be a possibility for encountering fluid elements which have already been emptied, and the prey flux becomes smaller. The flux depletion due to this effect increases for increasing radii in the reference volume. In order to have a moderate uncertainty on our estimators, we restrict the analysis to time intervals smaller than 2 s. A single predator with a small range, R, has only few possibilities for encountering prey in this time interval. We here present averages over many realizations and can therefore give accurate estimates nonetheless.

The 'fixed angle' case analyzed before may not be directly relevant for aquatic micro-organisms. In some cases arguments for varying orientation with respect to the flow vector can be given (Visser and Jonsson, 2000), this variation being either random or systematic. In the latter case, means are required for the organisms to sample the local flow velocity direction, and adjust to it almost instantaneously. Evidence can be found of rapid sensing of local flow conditions (Fields and Weissburg, 2005), although it is uncertain how rapidly micro-organisms are able to reorient in the flow.

In order to present results more general than those given in the previous section, we let here the angle between the local flow vector and the cone axis be

varying. The simplest means for this in the analysis is to let the symmetry axis of the cone be fixed in space. This would correspond, for instance, to a micro-organism facing a fixed light-source at all times. With the turbulence being homogeneous and isotropic to a good approximation, we will subsequently have the relevant angle be uniformly distributed over a unit sphere. We obtain results which resemble those in Fig. 3, but with somewhat different numerical values.

Dimensional reasoning

The problem of turbulent particle flux to a perfect absorber moving with the flow can be studied analytically by allowing for some simplifying assumptions. We can rely on simple dimensional arguments, or alternatively derive a dynamic model equation for the problem. This is usually possible only for some simple geometries. Here, we consider the case where an absorbing spherical surface is assumed to have its center defined by a particle, which is moving with the flow.

The present problem is characterized by a few dimensional quantities. With the viscosity ν being immaterial for the flow dynamics for scale lengths larger than the Kolmogorov length scale $\eta \equiv (\nu^3/\varepsilon)^{1/4}$, we only have one quantity characterizing the flow, namely the specific energy dissipation ε with dimension $length^2\ time^{-3}$, and the length scale $R < L_{\text{int}}$ characteristic for the particular problem, here a moving conical volume, including a sphere for $\theta = 180^\circ$. Out of these quantities the only combination giving a quantity with dimension *time* is $R^{2/3}/\varepsilon^{1/3}$, while $\varepsilon^{1/3}R^{7/3}$ gives $length^3\ time^{-1}$. We consider here ε as a deterministic quantity, and thereby ignore intermittency effects. The physical dimension of the averaged normalized particle flux $\langle \mathcal{J} \rangle / n_0$ is $length^3\ time^{-1}$, with n_0 being a constant. We have n_0 being the initial concentration, which for times up to 1–2 s is also the concentration at large distances from the reference volume of interception. Note that n_0 is different for the different realizations summarized in Table II. For the discussions in the present study the concentration (i.e. prey concentration) is trivial: a doubling of prey concentration gives here a doubling of the prey flux.

Quite generally it can then be argued, by purely dimensional reasoning (Buckingham, 1914), that the turbulent flux for given reference density n_0 must have the form

$$\frac{\langle \mathcal{J} \rangle}{n_0} = \varepsilon^{1/3} R^{7/3} f\left(\frac{t\varepsilon^{1/3}}{R^{2/3}}\right), \qquad (2)$$

with f being a dimensionless function of a dimensionless variable. The actual form of f can only be determined by a more detailed model analysis, and will also depend on the value for θ, here assumed constant. We can argue that we, in Fig. 3, have determined f experimentally, without reference to any explicit model equations. The arguments do not depend on any specific shape of the reference volume, and assume only that it scales self-similarly with one length scale, R. The functional dependence f in equation (2) will, of course, be different for different shapes of the volume. Note that for $t > R^{2/3}/\varepsilon^{1/3}$, see Fig. 3, the variation of $f(\tau)$ is rather slow for parameters relevant here. The observations summarized in Fig. 3 indicate that f approaches a constant value for large times. The constant is assumed to be universal, and for large θ, we find it to be in the range 5–10, as discussed in more detail later.

The scaling laws are most readily illustrated by considering compensated fluxes, i.e. the flux from Fig. 3 divided by $\varepsilon^{1/3}R^{7/3}$. With this normalization the ideal case will give a horizontal line for varying R or varying ε. The term 'compensated flux' is standard, but for the present case it can be interpreted as $f(\tau_0)$, with reference to equation (2). In Fig. 4a we show the compensated fluxes obtained at a fixed time $\tau_0 \equiv 0.9\ \tau_F$ for varying R, and different angles θ, all for the same ε -value. The 'eddy turnover time' $(R^2/\varepsilon)^{1/3}$ appropriate for the scale R is denoted τ_F. By this choice of τ_0 we have that all relevant times fall within the 2 s long time tracks where we have acceptable statistics.

In Fig. 4 we have results for compensated fluxes for the two orientations mentioned before. For the spherical case there should be no difference between the two cases, and indeed the two corresponding curves are identical. For the smallest angles, for instance $\theta = 30^\circ$ i.e. bottom curves in Fig. 4a and b, we find a nontrivial difference,

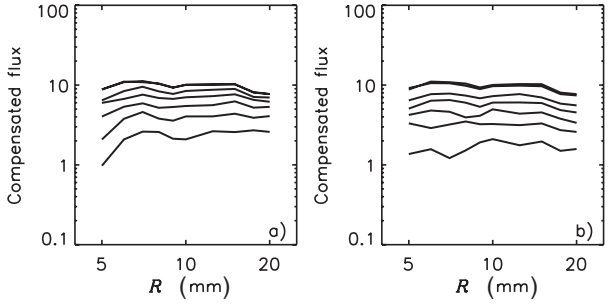

Fig. 4. Compensated flux to a moving conical volume, for varying radii R and opening angles $\theta = 30^\circ, 45^\circ, 60^\circ, 75^\circ, 90^\circ, 135^\circ$ and a full sphere $\theta = 180^\circ$. The smallest θ-value corresponds to the lowest curves and increases successively. The difference between the curves for $\theta = 135^\circ$ and $\theta = 180^\circ$ is negligible. In panel (**a**) we have the axis of the cone being parallel to the local velocity vector at all times and in panel (**b**) the cone axis is fixed with respect to the laboratory frame. Fluxes are obtained systematically at a time corresponding to $\tau_0 = 0.9\ \tau_F$, where the appropriate eddy turnover time is given as $\tau_F = (R^2/\varepsilon)^{1/3}$. We have $\epsilon = 225\ \text{mm}^2\ \text{s}^{-3}$. The irregularities of the individual curves represent the statistical uncertainties.

the flux in Fig. 4b being only ~1/2 of the corresponding flux in Fig. 4a. This feature will be discussed in more detail later on. For small R-values we note some irregularities in the curves in Fig. 4; these are due to statistical uncertainties caused by the reduced number of particles entering the averages when the test-volumes become small. Also we note that even though R is larger than the Kolmogorov scale, we might have the transverse dimension of the cone to be small when the opening angle θ in the cone is small. In particular we might have cases where a particle representing prey enters and then leaves the cone within one sampling time, 1/25 s, in which case it is not counted.

In Fig. 5 we show the compensated flux variation for a fixed angle $\theta = 60^\circ$, and varying radii R. In Fig. 5a we have the cone axis being parallel to the local flow velocity vector. Here we use the results for all eight realizations summarized in Table II. The six values of ε = 62, 65, 135, 140, and the two realizations of 160 mm^2 s^{-3} cluster in the middle of the figure, the two largest values ε = 225 and 279 mm^2 s^{-3} are the two top ones. We have analyzed several other values of θ as well, and find results like those shown in Fig. 5, although the statistical scatter increases with small θ, as expected. Within the uncertainty on the value for the specific energy dissipation rate ε, we find that the proposed $\varepsilon^{1/3}R^{7/3}$ scaling of the flux is well satisfied for all θ.

In Fig. 5b we show the compensated flux variation for a fixed angle $\theta = 60^\circ$, and varying radii R, with the cone axis being fixed in space. We use again the results for all eight realizations summarized in Table II. Note that the two Fig. 5a and b are close to identical, apart from a difference in the magnitude of the flux, as consistent with Fig. 4a and b. The factor 10^5 mentioned with Fig. 3 is now included in the numbering on the vertical axis. If the scaling law $\varepsilon^{1/3}R^{7/3}$ implied in equation (2) was ideally satisfied, the lines should be identical and horizontal in Fig. 5a and b. It is close to be so, and the deviations from the ideal case are within our experimental uncertainties, here mainly on ε.

As a consequence of results summarized in Fig. 5, we can state that a given predator, here defined by constant R and θ, is experiencing a variation of the prey flux as $\varepsilon^{1/3}$ when exposed to different turbulence levels. Since the physical conditions (and the local flow symmetry conditions in particular) for the data analysis in Fig. 5a and b are different, we had anticipated that slight differences could be found between the proposed scalings, apart from the difference in the numerical constant, as observed. Should such a difference exist, it is below the accuracy of our measurements, where we again expect the uncertainty on ε to be most important. Numerical simulations may help to resolve this question.

To make the difference between the two limiting cases of cone-orientations more clear, we show in Fig. 6 the flux variation for fixed R and varying θ. The two symbols, open and filled circles, show the cases with directions being fixed with respect to the flow vector and the laboratory frame, respectively. In this representation it is quite evident that for the orientation being fixed with respect to the local flow the fluxes are consistently above those for the other case, with orientations varying randomly with respect to the local velocity vector of the flow. The trivial exception is the spherical case, $\theta = 180^\circ$.

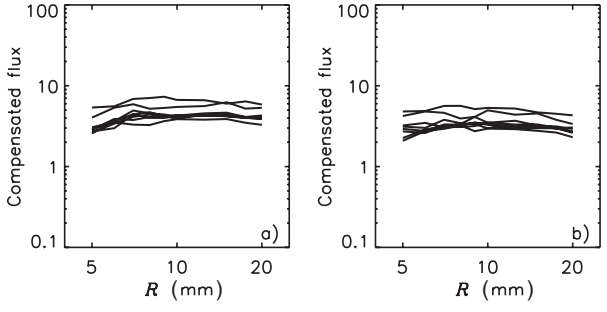

Fig. 5. Compensated fluxes, $\langle \tilde{f} \rangle / (n_0\ \varepsilon^{1/3}R^{7/3})$, to a moving conical volume, for varying radii R and a fixed opening angle $\theta = 60^\circ$, and eight realizations of turbulence conditions. The fluxes are sampled at the same times τ_θ as in Fig. 4. In panel (**a**), the cone axis is aligned with the local flow velocity vector at all times, whereas in panel (**b**) the direction is fixed in the laboratory frame.

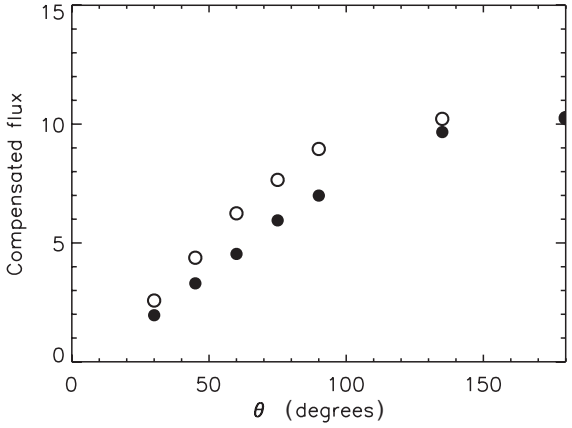

Fig. 6. Compensated asymptotic fluxes into a cone for R = 15 mm, for varying θ. The case where the direction of the cone axis is at all times aligned with the local flow velocity vector is marked by open circles; the case where the direction of the cone axis is fixed in the laboratory frame has filled circles. We have ε = 225 mm^2 s^{-3}.

A model diffusion equation

The particle flux to a perfectly absorbing spherical volume, which is moving with the flow, has been modeled by, for instance, a simple diffusion equation with a properly chosen diffusion coefficient which depends on the simultaneous mean square velocity differences obtained at given spatial separations, but independent of time (Osborn, 1996). Essentially, the argument is based on the second order structure function [equation (1)], with the approximation being valid for separations r smaller than the length scale of the turbulence. A dimensionally correct diffusion coefficient was constructed by multiplying a characteristic velocity and a characteristic length, see also Table I. The velocity was taken to be $\sqrt{\Psi_2(r)}$. For the limiting form expressed in equation (1), the only length characterizing the two particles is their separation r. The resulting diffusion coefficient is consequently $K(r) \sim r^{4/3}\varepsilon^{1/3}$. The proposed diffusion equation for the density n is actually identical to the one suggested by Richardson in his study of distance-neighbor functions (Richardson, 1926)

$$\frac{\partial}{\partial t}n(r,t) = C\frac{\varepsilon^{1/3}}{r^2}\frac{\partial}{\partial r}r^{10/3}\frac{\partial}{\partial r}n(r,t). \qquad (3)$$

The result is written for the assumed spherically symmetric geometry, with r being the radial coordinate, measured from the position of the center of the reference sphere, and C is a numerical constant, assumed to be universal. While equation (3) was here argued in part by dimensional reasoning, it has also an analytical derivation (Roberts, 1961). As expected, the solutions to equation (3) follow the dimensional scaling obtained by equation (2).

The model equation (3) assumes, as stated, spherical symmetry, and the flux to a spherical absorber obtained by solving equation (3) has been compared with experimental results (Mann *et al.*, 2005). The time-asymptotic evolution showed reasonable agreement qualitatively as well as quantitatively. If we consider surfaces without the spherical symmetry, equation (3) becomes inapplicable, and it is not easy to allow for arbitrary shapes. As far as the dimensionally argued result [equation (2)] is concerned, each new surface implies that a new function f has to be found with a new asymptotic limit, but the scaling with R and ε remains applicable, where it is implicitly assumed that the scaling with R is carried out in a way that preserves the shape of the volume, and only vary its scale size.

Again, we note that the results from the previous section have a wider range of applicability, and need not refer explicitly to spherical forms. A change in shape of the reference volume will only imply a change in the numerical constant. Thus, the scaling law implied in equation (2) is expected to apply, for instance, to the prey flux for any predator, independent of the shape of the interception volume, when it is exposed to different turbulence intensities as given by ε.

Given the experimental uncertainties, the scaling relations obtained by dimensional reasoning are found to be well satisfied when analyzing the data from our experiment. The more specific diffusion equation model [equation (3)] for the spherically symmetric case, is only giving qualitative agreement for the measured Lagrangian fluxes. It seems, however, that the asymptotic limit is reasonably well accounted for by the model, in particular also the numerical coefficient obtained by use of the most recent experimentally obtained value of the Richardson constant (Ott and Mann, 2000), see also numerical results by Boffetta and Sokolov (Boffetta and Sokolov, 2002).

Space-time variation of particle concentrations

As particles are absorbed by the surface, the particle density will be depleted in the flow surrounding the moving reference volume. Inside the volume we find trivially a vanishing particle concentration for $t > 0$. We can analyze the radial variation of the average particle density as a function of time, with results shown in Fig. 7a. The radius R is chosen to be in the universal subrange. The first curve is shown at the first sampling time, i.e. $t = 1/25$ s. Variations with distance are obtained in 'bins' of 1 mm, and the second bin from the center is the first one shown. To reduce the noise level, we normalized also here the curves with the radial density variation found at $t = 0$. Results corresponding to those in Fig. 7a, but now

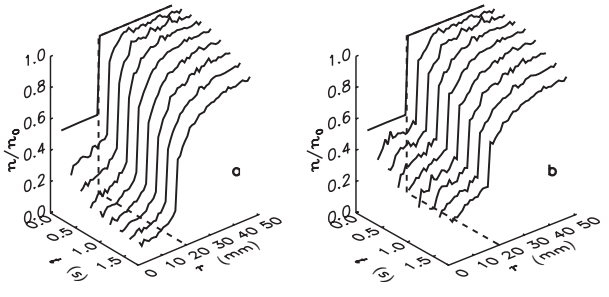

Fig. 7. Space-time evolution of the normalized density around an absorbing conical surface moving with the flow, here for $\theta = 90^\circ$ and $R = 20$ mm. The cone axis is along the local flow vector at all times in panel (**a**) and fixed in the laboratory frame in panel (**b**). The spatial variation is averaged over all the spherical angles, to give a representation in terms of r only. By this construction, we evidently have the normalized concentration to be 1/2 for $r < R$ at $t = 0$, for the present case with $\theta = 90^\circ$.

with varying angles between cone axis and flow vector are shown in Fig. 7b for comparison. These results also serve to demonstrate that a predator affects the local average prey density up to distances 2–3 R. At larger distances, the turbulent mixing is effective in replenish the prey being captured. (In one or two spatial dimensions this may be different (Mann *et al.*, 2003))

Experimental results for the variation of particle fluxes over the surface

With the available information, we are in a position to analyze the distribution of the particle fluxes over the absorbing surfaces. It is, for instance, simple to distinguish particles entering the spherical parts and the conical parts, see for instance Fig. 1c. The observations are summarized in Fig. 8. The results for the present case are somewhat counterintuitive by demonstrating that just as much of the particle flux is into the spherical part [with surface $S_s = 2\pi R^2 (1 - \cos\theta)$], as to the conical part (with surface $S_c = \pi R^2 \sin\theta$). The ratio of the two surfaces is $S_s/S_c = 2(1 - \cos\theta)/\sin\theta$. For small θ we have $S_s/S_c \approx \theta$, while $S_s/S_c = 1$ for $\theta \approx 60°$. In Fig. 8 we have $\theta = 30°$, and consequently $S_s/S_c = 2(2 - \sqrt{3}) \approx 0.54 < 1$, i.e. the spherical part has the smallest area, but after a short transient time interval it carries as much flux as the conical part. The implications are that with the cone axis along the local velocity vector, it is the size of the surface in the field of view facing the flow that is most important for determining the prey flux to the surface. As far as the accessible prey flux is concerned, this result implies that a micro-organism has an optimum orientation with respect to the local velocity vector in a turbulent flow. To take advantage of this, it is, however, necessary that it possesses an ability to change and maintain orientations with respect to the local turbulent velocity field. The gain by such an ability is, however, relatively modest and can for given θ be estimated by the difference between the ordinates for the filled and open circles in Fig. 6, where the open circles corresponds to the limiting case with an organism constantly aligned with the local flow vector, while filled symbols refer to an organism 'tumbling' randomly in the flow. The observation seems to be in variance with the given homogeneity and isotropy of the flow. This objection is in error, however, because we consider here a conditionally selected flow, with the cone axis pointing along the local flow velocity at all times. If we instead, as in Fig. 4b, let the angle between the velocity vector and the cone axis vary, we find results as in Fig. 9. In this case, the axis of the cone is 'tumbling' with respect to the local velocity vector, and we have no simple analytical expressions for comparison. For this case the spherical part of the surface is facing the flow just as often as the conical part. When the cone is facing the flow 'sidewise' it is the conical part that receives the largest flux, the projection of the spherical part of the surface being generally small, in this case. We note that in Fig. 9 the ratio between the fluxes to the spherical and conical parts of the surface has an approximately constant ratio of ~ 0.5. The present discussion also explains the difference between the results of Fig. 4a and b for the smallest opening angles, θ.

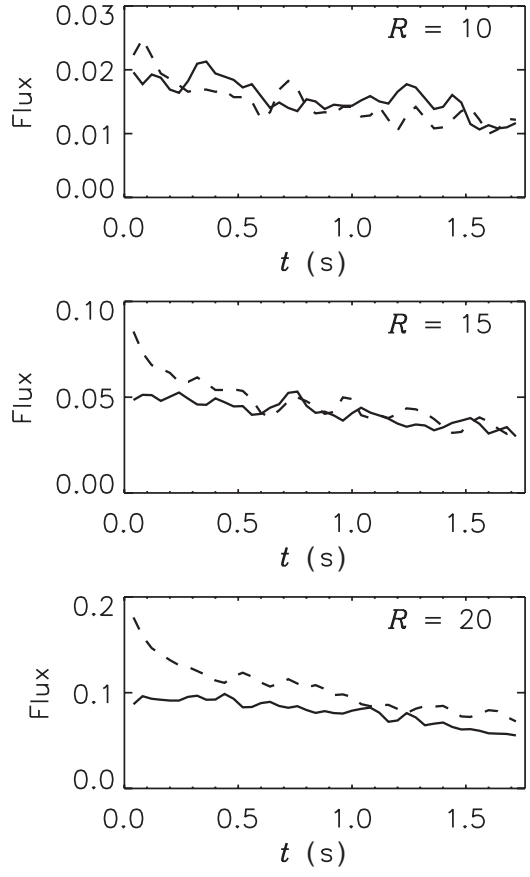

Fig. 8. Time variations of the fluxes into the spherical (full lines) and the conical (dashed lines) parts of the reference volume, for R = 10, 15 and 20 mm, here for the case with $\theta = 30°$. For this case, we have the direction of the cone axis to be aligned at all times with the velocity vector at the reference particle.

The results of Fig. 7a illustrate how the particle density in the wake of a cone with 90° opening angle (a half sphere) is depleted with time, for the case where the cone-axis is aligned with the local flow vector. We find a decay time in excess of 1 s. If the angle between the cone axis and the local flow velocity vector is allowed to vary as in Fig. 7b, we find the particle density in the wake of the half-sphere to be larger for $r < R$, because particles are continuously 'mixed-in' from the surroundings. The case where the predators field-of-view has an opening

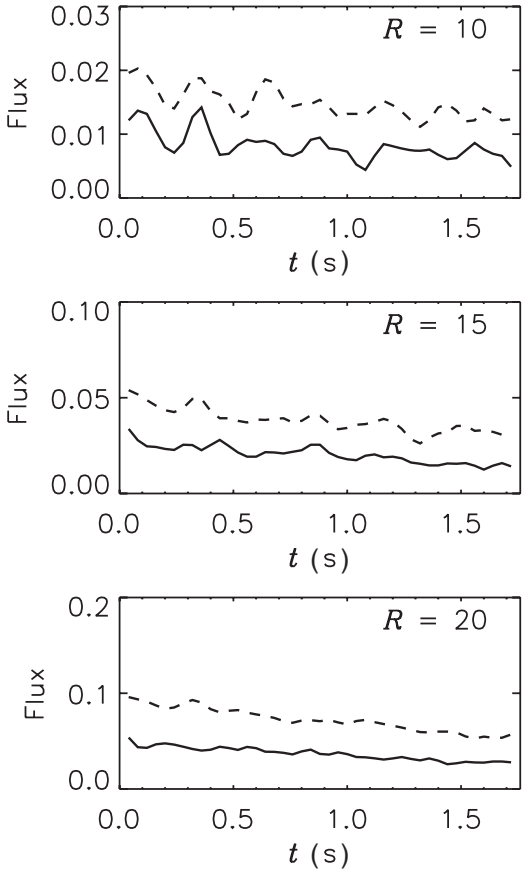

Fig. 9. Time variations of the fluxes into the spherical and the conical parts of the reference volume, for R = 10, 15 and 20 mm, for the case with $\theta = 30^\circ$ as in Fig. 8. For the present case, we have the direction of the cone axis to be fixed in space, so that the angle between this axis and the local flow vector is randomly varying over all angles. Full line gives the flux to the spherical part and the dashed lines to the cone.

angle of $\theta = 90^\circ$ has received particular attention in other studies (Lewis and Pedley, 2001).

The full space-time variation of the flow field and corresponding particle flux densities in the spatial region surrounding the reference particle is evidently not available, only the statistical average. We can however, obtain related information which turns out to explain the essential parts of the observations summarized in Figs 8 and 9. We can thus find an analytical expression for the conditionally averaged flow field in a volume surrounding a reference particle, subject to the condition that the particle velocity vector is U. The essential parts of the analysis are given by Adrian (Adrian, 1979). The idea is to express the estimate for the conditionally averaged velocity field as a series expansion of the velocity components, $w_i = \Sigma_j A_{i,j} U_j + \Sigma_{j,k} B_{i,j,k} U_j U_k + ...$, where the conditioned vector **U** is taken from the realizations of the flow, and will therefore have the same statistical distributions as the fluid velocity u. The space-time varying coefficients $A_{i,j}$, $B_{i,j,k}$, etc., are subsequently determined by minimizing the mean square error $e_i \equiv \langle (w_i - u_i)^2 \rangle$ by standard methods (Adrian, 1979, 1994). In order to obtain a closed set of equations, it is necessary to truncate the series expansion implied in w_i. If we truncate the series after the second term, the results are expressed in terms of the velocity correlation functions and the triple correlation function, as

$$A_{i,j}(r,t) = \frac{1}{\sigma^2}\left\langle u_j(\mathbf{x},t_0)u_i(\mathbf{x}+\mathbf{r},t_0+t)\right\rangle \qquad (4)$$

and

$$B_{i,j,k}(r,t) = \frac{3}{2K\sigma^4}\left\langle u_k(\mathbf{x},t_0)u_j(\mathbf{x},t_0)u_i(\mathbf{x}+\mathbf{r},t_0+t)\right\rangle \quad (5)$$

assuming homogeneous and isotropic turbulence, with $\sigma^2 = 1/3\langle u^2\rangle$ and K being the kurtosis (Adrian, 1979; Tung and Adrian, 1980). The present inclusion of space as well as time variation of the coefficients $A_{i,j}$, $B_{i,j,k}$ implies a slight generalization (Guezennec, 1989) of the results by Adrian (Adrian, 1979). It can be demonstrated that $A_{i,j}$ can be expressed in terms of $f(r,t) = \langle u_{||}(\mathbf{x},t_0)\, u_{||}(\mathbf{x}+\mathbf{r},t_0+t)\rangle/\sigma^2$, where the subscript $_{||}$ indicates components $_{||}$ r. Similarly, it can be shown that $B_{i,j,k}$ can be expressed in terms of $k(r,t) = \langle u_{||}^2(\mathbf{x},t_0)\, u_{||}(\mathbf{x}+\mathbf{r},t_0+t)\rangle / \sigma^3$ (Batchelor, 1953). For $t = 0$, we can use the Kolmogorov–Oubokhov law $f(r,0) \approx 1 - C_K(\varepsilon r)^{2/3}/\sigma^2$. Similarly, for small r, we can approximate $k(r,0) \approx -\alpha\varepsilon r/\sigma^3$, using the value $\alpha \approx 0.1$ as obtained from experimental observations (Van Atta and Chen, 1970) rather than the 4/5 Kolmogorov law, which is supposed to be exact only in the limit of infinite Reynolds numbers.

The results of this method of estimation have been tested also for significantly non-Gaussian signals, showing good agreement even with relatively few terms retained in the series expansion for the estimator (Pécseli and Trulsen, 1989, 1991). It turns out that the method reproduces exact results for Gaussian random processes (Papoulis, 1991).

In Fig. 10 we show results for the conditionally averaged flow in the rest frame, while in Fig. 11, it is transformed into the frame of reference following the selected particle. For the case given here we have $U = 2\sigma$. It turns out that the contribution from $k(r)$ is insignificant unless we have very large values for the imposed condition, $U > 5\sigma$. In other words: for the most probable velocities the linear estimate will suffice, as based on equation (4). In Fig. 12 we show selected particle trajectories obtained by following particles released in the conditionally averaged flow field shown in Fig. 11. For illustrative purposes, we assumed a time variation of $f(r,t)$ and $k(r,t)$ by simply

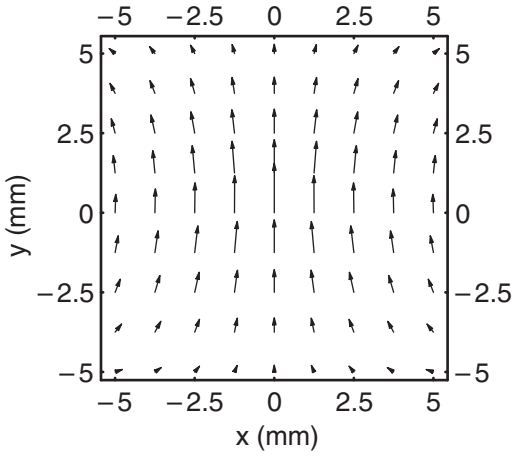

Fig. 10. Conditionally averaged velocity field around a moving reference particle at $t = 0$, here shown for the condition $U = 2\sigma$. The figure is shown in the laboratory rest-frame. The length of the arrow at the origin gives the scale as determined by the imposed condition, U.

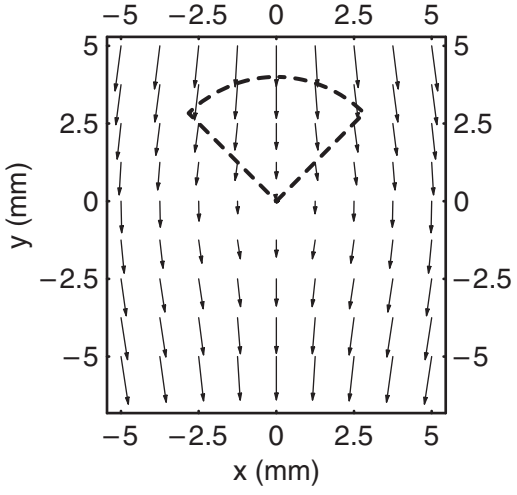

Fig. 11. Conditionally averaged velocity field around a moving reference particle at $t = 0$, here shown for the condition $U = 2\sigma$. The figure is shown in the frame following the reference particle and represents the average flow field observed by the predator. A small cone is inserted with dashed lines, to illustrate the predator field of view, here with $\theta = 45^\circ$ and $R = 4$ mm. Note that the figure frame is vertically asymmetric, in order to make space for the arrows.

introducing a multiplying exponential factor with a decay time given by the correlation time. This approximation will be too simplistic for a quantitative analysis, but serves here for illustration.

By inspection of Fig. 11 as well as Fig. 12 we readily find that given a conical surface having its axis aligned with the flow in these model flows, the particles will on average enter this surface through the part facing the flow vectors, i.e. the spherical segment in this case. In actual realizations of the flow, we of course have

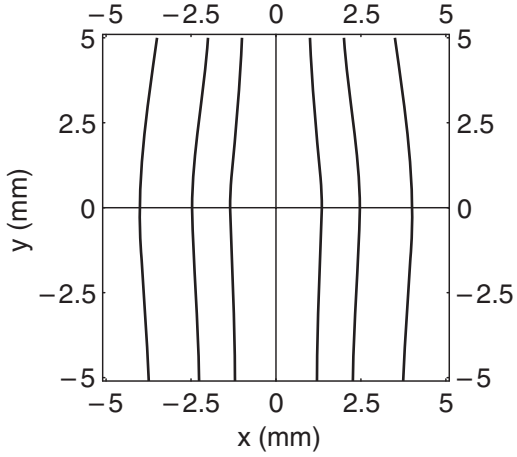

Fig. 12. Particle trajectories calculated for the conditionally averaged velocity field shown in Fig. 11. The particles are released in the top of the figure.

fluctuations in addition to this conditional average, and some particles will enter through the conical back surface as well, as found in Fig. 8.

CONCLUSIONS

We have analyzed turbulent particle fluxes to moving conical surfaces using data from a laboratory experiment, letting such surfaces represent the 'surface of interception' of aquatic micro-organisms. Several flow conditions were analyzed and the results compared. It was demonstrated that the asymptotic normalized flux to a surface, $\langle \mathcal{J} \rangle / n_0$, scales with $\varepsilon^{1/3} R^{7/3}$, in terms of the radius in the cone R and the turbulence level as measured in terms of the energy dissipated per unit mass of fluid, ε, see Fig. 5. The most important new result of the present study is an experimental verification of this universal scaling, demonstrating in particular that it remains valid also for general shapes and orientations of the field of vision of the predator. The scaling with turbulence intensity, as measured by ε is weak: it requires an eight times increase in ε to double the prey flux. On the other hand, the flux increases with R faster than the surface of the volume of interception.

The dimensionless function $f(\tau)$ entering equation (2) can be determined empirically from results like those shown in Fig. 3, as illustrated, for instance, by Mann *et al.* (Mann *et al.*, 2005) for spherical search volumes. The only essential distinction between the various surface forms, as far as the scaling law is concerned, lies in different numerical factors, which consequently depend on θ, where empirical results can be derived from Fig. 6. For a sphere the numerical factor $C_F \equiv f(\tau \to \infty)$ is in the

range 4–9, and for a cone the corresponding number is obtained by multiplying C_F with the ratio of the compensated flux for the corresponding θ in Fig. 6, and the corresponding flux for the sphere, i.e. $\theta = 180^\circ$. As an approximation for $20^\circ \leq \theta \leq 100^\circ$, we can use the empirical correction factor $(\theta - 10^\circ)/120^\circ$, with θ inserted in degrees, obtained by inspection of Fig. 6 using the filled circles. The proposed $\varepsilon^{1/3}R^{7/3}$ scaling was previously predicted and then demonstrated for spherical surfaces, but it is evidently not restricted to this simple geometry. Formally, the suggested scaling can be obtained as a product of a reference area and a velocity, as also discussed before. As long as we are concerned with spherical geometries, the relevant area is easily determined, but as soon as the assumption of simple geometry is relaxed, the relevant effective area is no longer evident. Similar comments apply to the characteristic velocity. The results of Fig. 6 support also the observations by Galbraith *et al.* (Galbraith *et al.*, 2004) who compared a 'wedge-shaped' field of view with a hemispherical model ($\theta = 90^\circ$ in our model) in their net energy gain model, and found an increase in prey capture rate by approximately a factor three.

The previous dimensional analysis assumed the dissipated energy per mass fluid to be a deterministic quantity, thereby ignoring intermittency corrections (Boffetta and Sokolov, 2002). With ε being statistically varying with spatial as well as temporal variables, we have $\langle\varepsilon^{1/3}\rangle \neq \langle\varepsilon\rangle^{1/3}$, for instance, and it is not obvious how to interpret the proposed scaling law in equation (2). We here identified ε by the value found by fitting the universal Kolmogorov–Oubokhov law [equation (1)] to the experimentally obtained second order structure function. We note a nontrivial uncertainty in the estimate, and also that other methods of definition could be used as well (Mann *et al.*, 1999). The average value $\langle\varepsilon\rangle$ is the most obvious choice in equation (2): this quantity is easy to define, but unfortunately difficult to determine experimentally. Numerical simulations have a significant advantage in this respect. It is in principle possible to obtain $\langle\varepsilon\rangle$ by the third order structure function (Van Atta and Chen, 1970). This result is exact only in the limit of infinite Reynolds numbers, and no existing controlled laboratory experiments reach a parameter regime where this expression can be used, not even as an approximation.

Self-induced motion of predators will be important for quiet environments, i.e. small ε. The dataset does not allow a modeling of predator motion, and this problem will presumably best be studied by numerical flow simulations. We have implicitly assumed prey to be captured with certainty, which also represents an approximation. This question can be more easily studied within the available database, as illustrated by Mann *et al.* (Mann *et al.*, 2003), but requires some a priori model for capture probability in terms of, say, the transit time of prey through the capture region. For the spherical reference case, we have empirical models for the probability densities of these transit times, and a model can be formulated in terms of these (Mann *et al.*, 2003; Jørgensen *et al.*, 2005). By this, we believe that it is possible to model changes in behavior of the micro-organisms caused by the turbulence level in the environment.

The universal normalized flux function $f(\tau)$ in equation (2), has a constant asymptotic value for R in the universal subrange, for the spherical case $f(\infty) \approx 4$–9, as stated before (Mann *et al.*, 2005). The initial value, $f(0)$, is approximately twice this value, although this estimate has a nontrivial uncertainty. (Note that R for the top curve in Fig. 3 is outside the universal subrange.) The physical reason for the reduction in flux from $f(0)$ to $f(\infty)$ is that initially the predator is immersed in the maximal prey concentration. At later times this concentration is depleted in its near environment as seen from, for instance, Fig. 7, and the asymptotic flux $f(\tau\rightarrow\infty) = C_F$ is determined by the balance of captured prey, and the transport of 'fresh prey' into the search volume due to the turbulent mixing in the flow. A 'jump-pause' predator can move into a fresh fluid volume, which has not been searched for prey previously, by jumping a distance l. Inspection of Fig. 7 indicates that $l/R \sim 3$–4 suffices for this. In the 'pause' phase the predator is moving with the flow, and captures a prey-flux as the one illustrated in Fig. 3, starting at a value $n_0\,\varepsilon^{1/3}R^{7/3}f(0)$. The ratio $f(0)/f(\infty)$ (where the dimensional coefficient $n_0\,\varepsilon^{1/3}R^{7/3}$ cancels), is a measure for the maximum gain by this strategy. The precise numerical value for this gain is presumably found best by numerical simulations.

We find a noticeable difference between the two limiting cases for the orientation of the predator considered here, i.e. the one with cone axis parallel to the local flow vector in Fig. 6 (open circles) and the other where the direction with respect to the local flow changes randomly (filled circles in Fig. 6). The variation has been analyzed for all available realizations summarized in Table II, and found to be consistent. In a general sense, the results illustrate the effect of the orientation of micro-organisms with respect to the flow field. We found that the gain in changing from a random orientation to the optimum case can be at most 30 % for small angles in the reference cone. This can be seen as the maximum gain a micro-organism could obtain if given the capability of orienting itself (at least somewhat) with respect to the local flow velocity vector. From a physical point of view, we find the difference between the two orientations analyzed here to be interesting, and also somewhat

counterintuitive. The difference was explained by introducing the conditionally averaged flows, see Figs 10 and 11, and it is plausible that such models can be useful in other contexts as well.

ACKNOWLEDGEMENTS

This work was in part supported by the Danish Technical Research Council under contracts STVF-9601244 and 26-01-0087. Two of the authors (HLP and JT) were in part supported by the 'Effects of North Atlantic Climate Variability on the Barents Sea Ecosystem' (ECOBE) project. The present study was carried out while two of the authors (HLP and JT) were affiliated with the Norwegian Center for Advanced Studies under the project 'Turbulence in Fluids and Plasmas'. We thank Jan Erik Stiansen and Øyvind Fiksen for valuable comments on the manuscript.

REFERENCES

Adrian, R. J. (1979) Conditional eddies in isotropic turbulence. *Phys. Fluids*, **22**, 2065–2070.

Adrian, R. J. (1994) Stochastic estimation of conditional structure: a review. *Appl. Sci. Res.*, **53**, 291–303.

Batchelor, G. K. (1953) *The Theory of Homogeneous Turbulence*. Cambridge University Press, Cambridge, England.

Blaxter, J. H. S. and Staines, M. E. (1971) Food searching potential in marine fish larvae. In Crisp, D. J. (ed.), *Proceedings of the 4th European Marine Biology Symposium*. Cambridge University Press, UK, pp. 467–485.

Boffetta, G. and Sokolov, I. M. (2002) Relative dispersion in fully developed turbulence: the Richardson law and intermittency corrections. *Phys. Rev. Lett.*, **88**, 094501.

Browman, H. I. (1996) Predator-prey interaction in the sea: commentaries on the role of turbulence. *Mar. Ecol. Prog. Ser.*, **139**, 301–312.

Buckingham, E. (1914) On physically similar systems; illustrations of the use of dimensional equations. *Phys. Rev.*, **4**, 345–376.

Bundy, M. H., Gross, T. F., Vanderploeg, H. A. *et al.* (1998) Perception of inert particles by calanoid copepods: behavioral observations and a numerical model. *J. Plankton Res.*, **20**, 2129–2152.

Fields, D. M. and Weissburg, M. J. (2005) Rapid firing rates from mechanosensory neurons in copepod antennules. *J. Comp. Physiol. A*, **190**, 877–882.

Galbraith, P. S., Browman, H. I., Racca, R. G. *et al.* (2004) Effect of turbulence on the energetics of foraging in Atlantic cod *Gadus morhua* larvae. *Mar. Ecol. Prog. Ser.*, **281**, 241–257.

Gerritsen, J. and Strickler, J. R. (1977) Encounter probabilities and community structure in zooplankton: a mathematical model. *J. Fish. Res. Board Can.*, **34**, 73–82.

Granata, T. C. and Dickey, T. D. (1991) The fluid mechanics of copepod feeding in turbulent flow: a theoretical approach. *Prog. Oceanogr.*, **26**, 243–261.

Guezennec, Y. G. (1989) Stochastic estimation of coherent structures in turbulent boundary layers. *Phys. Fluids A.*, **1**, 1054–1060.

Hinze, J. O. (1975) *Turbulence*, 2nd edn. McGraw-Hill, New York.

Hwang, W. and Eaton, J. K. (2004) Creating inhomogeneous and isotropic turbulence without a mean flow. *Exp. Fluids* **36**, 444–454.

Jørgensen, J. B., Mann, J., Ott, S., Pécseli, H. L. *et al.* (2005) Experimental studies of occupation and transit times in turbulent flows. *Phys. Fluids.*, **17**, 035111.

Kiørboe, T. and MacKenzie, B. R. (1995) Turbulence-enhanced prey encounter rates in larval fish: effect of spatial scale, larval behaviour and size. *J. Plankton Res.*, **17**, 2319–2331.

Kiørboe, T. and Saiz, E. (1995) Planktivorous feeding in calm and turbulent environments, with emphasis on copepods. *Mar. Ecol. Prog. Ser.*, **122**, 135–145.

Lewis, D. M. and Pedley, T. J. (2000) Planktonic contact rates in homogeneous isotropic turbulence: theoretical predictions and kinematic simulations. *J. Theor. Biol.*, **205**, 377–408.

Lewis, D. M. and Pedley, T. J. (2001) The influence of turbulence on plankton predation strategies. *J. Theor. Biol.*, **210**, 347–365.

Lewis, D. M. (2003) Planktonic encounter rates in homogeneous isotropic turbulence: the case of predators with limited fields of sensory perception. *J. Theor. Biol.*, **222**, 73–97.

MacKenzie, B. R., Miller, T. J., Cyr, S. *et al.* (1994) Evidence for a dome-shaped relationship between turbulence and larval fish ingestion rates. *Limnol. Oceanogr.*, **39**, 1790–1799.

Mann, J., Ott, S. and Andersen, J. S. (1999) *Experimental Study of Relative, Turbulent Diffusion, Technical Report Risø-R-1036 (EN)*. Risø National Laboratory, DK-4000 Roskilde, Denmark. http://www.risoe.dk/rispubl/VEA/ris-r-1036.htm

Mann, J., Ott, S., Pécseli, H. L. *et al.* (2002) Predator-prey encounters in turbulent waters. *Phys. Rev. E.*, **65**, 026304.

Mann, J., Ott, S., Pécseli, H. L. *et al.* (2003) Experimental studies of occupation times in turbulent flows. *Phys. Rev. E.*, **67**, 056307.

Mann, J., Ott, S., Pécseli, H. L. *et al.* (2005) Turbulent particle flux to a perfectly absorbing surface. *J. Fluid Mech.*, **534**, 1–21.

Mauchline, J. (1998) The biology of calanoid copepods. *Adv. Mar. Biol.*, **33**, 1–710.

Muelbert, J. H., Lewis, M. R. and Kelley, D. E. (1994) The importance of small-scale turbulence in the feeding of herring larvae. *J. Plankton Res.*, **16**, 927–944.

Osborn, T. (1996) The role of turbulent diffusion for copepods with feeding currents. *J. Plankton Res.*, **18**, 185–195.

Ott, S. and Mann, J. (2000) An experimental investigation of the relative diffusion of particle pairs in three dimensional turbulent flow. *J. Fluid Mech.*, **422**, 207–223.

Papoulis, A. (1991) *Probability, Random Variables and Stochastic Processes*, 3rd edn. McGraw-Hill, New York.

Pécseli, H. L. and Trulsen, J. (1989) A statistical analysis of numerically simulated plasma turbulence. *Phys. Fluids B.*, **1**, 1616–1636. [Erratum: (1990) *Phys. Fluids B.*, **2**, 454]

Pécseli, H. L. and Trulsen, J. (1991) Analytical expressions for conditional averages: a numerical test. *Phys. Scripta* **43**, 503–507.

Richardson, L. F. (1926) Atmospheric diffusion shown as a distance-neighbour graph. *Proc. Roy. Soc. London, Ser. A*, **6**, 709–737.

Roberts, P. H. (1961) Analytical theory of turbulent diffusion. *J. Fluid Mech.*, **11**, 257–283.

Rothschild, B. J. and Osborn, T. R. (1988) Small-scale turbulence and plankton contact rates. *J. Plankton Res.*, **10**, 465–474.

Sundby, S. and Fossum, P. (1990) Feeding conditions of arcto-norwegian cod larvae compared with the Rothschild-Osborn theory on small-scale turbulence and plankton contact rates. *J. Plankton Res.*, **12**, 1153–1162.

Tennekes, H. and Lumley, J. L. (1972) *A First Course in Turbulence*. The MIT press, Cambridge, Massachusetts.

Tung, T. C. and Adrian, R. J. (1980) Higher order estimates of conditional eddies in isotropic turbulence. *Phys. Fluids*, **23**, 1469–1470.

Van Atta, C. W. and Chen, W. Y. (1970) Structure functions of turbulence in the atmospheric boundary layer over the ocean. *J. Fluid Mech.*, **44**, 145–159.

Visser, A. W. and Jonsson, P. R. (2000) On the reorientation of non-spherical prey particles in a feeding current. *J. Plankton Res.*, **22**, 761–777.

Webster, D. R., Brathwaite, A. and Yen, J. (2004) A novel laboratory apparatus for simulating isotropic oceanic turbulence at low Reynolds number. *Limnol. Oceanogr-Meth.*, **2**, 1–12.